Contribution of next-to-leading order and Landau-Pomeranchuk-Migdal corrections to thermal dilepton emission in heavy-ion collisions

Yannis Burnier* and Chiara Gastaldi†
Institut de Théorie des Phénomènes Physiques, EPFL, CH-1015 Lausanne, Switzerland
(Received 15 September 2015; revised manuscript received 2 March 2016; published 8 April 2016)

Recently lots of effort has been made to obtain the next-to-leading-order and Landau-Pomeranchuk-Migdal corrections to the thermal dilepton emission rate in perturbative QCD. Here we apply these results to the plasma created in heavy-ion collisions and see whether these corrections improve the comparison between theoretical calculations and experimental results for the invariant mass dependence of the dilepton emission rate. In particular, we simulate the quark-gluon plasma produced at the Relativistic Heavy Ion Collider at the Brookhaven National Laboratory and the Large Hadron Collider at CERN using $2+1$-dimensional viscous hydrodynamical simulations. We compare our results to those of the STAR experiment and comment on the need for a nonperturbative determination of the dilepton rate at low invariant mass.

DOI: 10.1103/PhysRevC.93.044902

I. INTRODUCTION

The theoretical study of quark-gluon plasma (QGP) [1,2] has applications in experiments based on ultrarelativistic heavy-ion collisions (HICs): gold ions are used at the Relativistic Heavy Ion Collider (RHIC) at the Brookhaven National Laboratory and lead ions are used at the Large Hadron Collider (LHC) at CERN.

Photon and dilepton pairs are excellent probes to use to study QGP [3]. In fact, as they interact electromagnetically, their cross section with the strongly interacting matter inside the QGP is small. Thus they leave the QGP and reach detectors without being rescattered and carry information from deep into the plasma phase [4,5]. Moreover we prefer dileptons to photons for two reasons: photons are produced from a bigger background of decays while leptons have a non-null invariant mass, M, which helps in disentangling various dilepton sources [6].

In fact, the dilepton background is also not small: dileptons are produced in every phase of HICs and in several types of processes [7]. Here we are interested in thermal dileptons [3] produced by the partonic interactions during the hydrodynamical expansion; these dileptons can tell us about the QGP properties. Thermal dileptons are produced mainly in quark-antiquark annihilation and Compton scattering processes and their contribution to the dilepton spectrum is important in the intermediate invariant mass range, $M \in [0.2, 2.5]$ GeV.

The first type of background we encounter consists of hadronic reactions at early times. They consist of jet-dilepton conversion from the initial hadronic scattering and the photoproduction processes. These are hard processes that contribute to the dilepton invariant mass spectrum in the high mass range ($M > 3$ GeV).

Second, particle decays imprint broad peaks in the spectrum, for instance, the contribution from the decay of open charm $c\bar{c} \to e^+e^-X$ is also very important in the intermediate mass range [8,9]. In the low mass range $0.6 < M < 1.1$ GeV, the decays of vector mesons, i.e. ρ, ω, and ϕ, give a sizable contribution to the invariant mass spectrum [5,8,9]. Finally, below $M < 0.2$ GeV, pion decays from the hadronic phase dominate.

A big effort has been made to study the thermal dilepton production from the QGP in perturbative QCD: Ref. [3] discusses the leading-order (LO), corrections for anisotropic plasma are given in Ref. [10], and Refs. [11,12] supply the passage from the LO to the next-to-leading-order (NLO) and Landau-Pomeranchuk-Migdal (LPM) corrections.

In this work we investigate whether higher-order corrections in perturbation theory can improve the agreement between theoretical calculations for the thermal dilepton emission and experimental results. In Sec. II, we introduce the theoretical background, in particular, how to compute the LO dilepton emission rate per unit four-volume and per unit four-momentum, what the effect of NLO and LPM corrections are, and how the invariant mass spectrum is computed. In Sec. III, we explain how we describe the hydrodynamical plasma evolution using SONIC and the details of the numerical computation for the invariant mass spectrum. In Sec. IV, we show our results and compare them to experimental data from the STAR experiment at the RHIC [5]. We then make analogous computations for the LHC in Sec. IV B and conclude in Sec. V.

II. DILEPTONS IN HEAVY-ION COLLISIONS

We recall here the perturbative QCD calculations of the dilepton rate and explain how to use them in the geometry of heavy-ion collisions. We use natural units when not stated otherwise and the metric signature is $(+,-,-,-)$. In perturbation theory, two distinct expansions are made, one in the electromagnetic coupling, where the LO is sufficient, and a second one in the strong coupling. In this work we discuss the validity of this second expansion in the case of the plasma created in heavy-ion collisions.

*yannis.burnier@epfl.ch
†chiara.gastaldi@epfl.ch

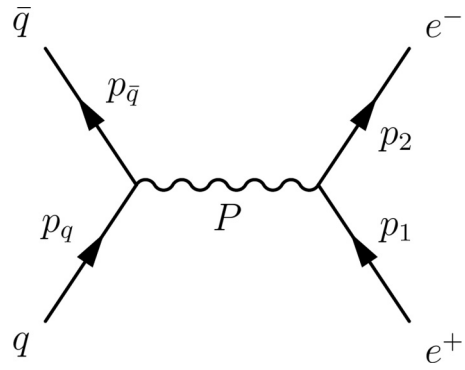

FIG. 1. LO Feynmann diagram for thermal dilepton production from QGP.

A. Leading-order dilepton production rate

The relation between the dilepton emission rate and thermal expectation values of the electromagnetic current correlation function

$$W^{\mu\nu} = \int d^4x\, e^{-iqx} \langle J^\mu(x) J^\nu(0) \rangle \tag{1}$$

is described in Refs. [3,13,14]. Here we briefly summarize the main results for the specific case of a $q\bar{q} \to e^+e^-$ process, shown in Fig. 1.

The number of dileptons produced per unit volume and emitted at a given total momentum $P = (p^0, p^i)$ can be expressed through the dilepton rate R:

$$\frac{dN^{\ell\bar{\ell}}(x,P)}{d^4x d^4P} = \frac{dR(x,P)}{d^4P}, \tag{2}$$

which in turn can be calculated form the quark current correlator $W^{\mu\nu}(P)$ as

$$\frac{dR^{\ell\bar{\ell}}}{d^4P} = \sum_{i=1}^{n_f} Q_i^2 \frac{\alpha_e^2}{24\pi^3 P^2}\left(1 + \frac{2m^2}{P^2}\right)\left(1 - \frac{4m^2}{P^2}\right)^{\frac{1}{2}} \times \theta\left(P^2 - 4m^2\right) W^\mu_\mu(P), \tag{3}$$

where m is the mass of the emitted leptons and $Q_i, i = 1, \ldots, n_f$, are the charges of the n_f massless quarks present in the plasma. The strong coupling only enters in the quark current correlator $W^{\mu\nu}(P)$, which is calculated below to the leading order but receives large higher-order corrections. If we restrict to leading order and to the case where the lepton mass is negligible compared to the invariant mass $M = \sqrt{P^2} \gg m$, which is a good approximation for electrons, we get [11]

$$\frac{dR^{\ell\bar{\ell}}_{\mathrm{LO}}}{d^4P} = \sum_{i=1}^{n_f} Q_i^2 \frac{\alpha_e^2}{2\pi^4} \frac{T}{p} \frac{1}{e^{E/T} - 1} \log \frac{\cosh \frac{E+p}{4T}}{\cosh \frac{E-p}{4T}}, \tag{4}$$

where $E = p_0$ and $p = p_i^2$.

B. NLO corrections to the spectra

As emphasized before, large corrections to the leading order dilepton rate arise. The NLO is suppressed only by α_s, but diverges in the small invariant mass limit $M \to 0$ (some representative diagrams for the NLO are shown in Fig. 2).

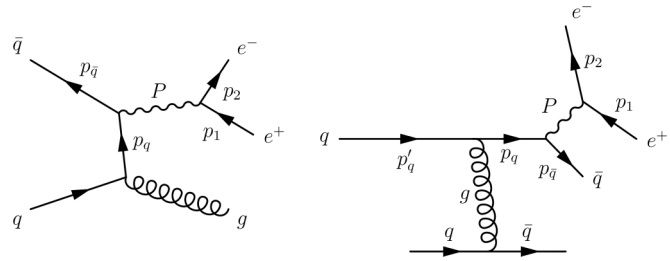

FIG. 2. Examples of NLO Feynman diagrams for thermal dilepton production from QGP.

In this soft limit a consistent result can only be obtained by performing the LPM resummation. The LPM resummation is a reorganization of perturbation theory that takes into account the destructive interference effects between the prompt emitted photons and is summarized by the Feynman diagram in Fig. 3.

In this section, we investigate how the NLO and LPM corrections contribute to the dilepton spectra. To show the results of NLO and higher-order corrections, we used the data provided by Ghisoiu and Laine [11] (NLO and LPM to LO) and Ghiglieri and Moore (for the LPM at NLO) [12]. It consists of a database for the electron-positron and the muon-antimuon emission rates as a function of the invariant mass M, the temperature T, and the modulus of three-momentum P for the NLO and the LPM corrections (available at Ref. [15]). Note that the cusp at $M/T = \pi$ is due to a change in the running of the renormalization scale $\mu = \min(M, \pi T)$ used in the previous references.

Figure 4 shows a comparison between the dielectron emission rate at LO computed with formula (4) and the same with NLO and NLO plus LPM corrections.

We can notice that the NLO and LPM contributions to the emission rate are important for small values of the ratio of the invariant mass over temperature, M/T. Surprizingly the LPM corrections increase the dilepton rate for intermediate values of the invariant mass. For small invariant mass, $M < T$, from the NLO + $\mathrm{LPM_{LO}}$ curve in Fig. 4, we see that the LPM effect works as it should and the NLO + $\mathrm{LPM_{LO}}$ curve is below the

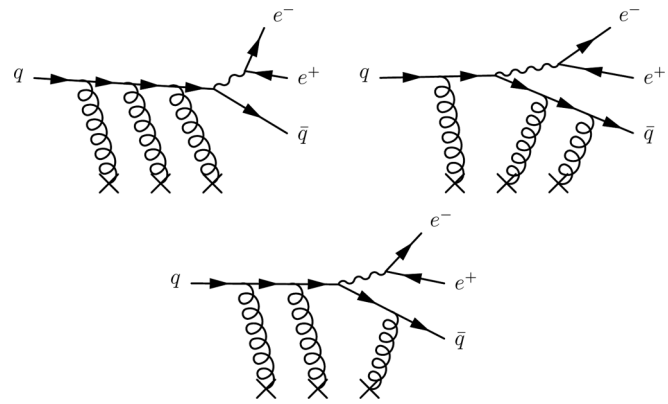

FIG. 3. Examples of Feynman diagrams that illustrate the LPM effect: in very dense QGP a slow quark is rescattered many times before and after emitting a photon. Destructive interferences between different diagrams damp the photon emission at low invariant mass.

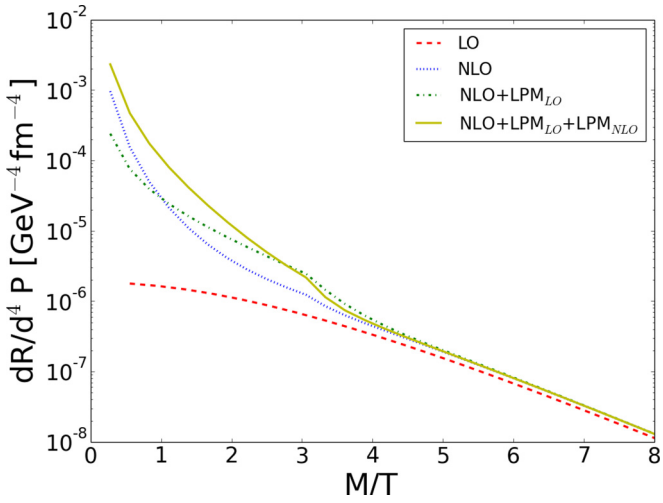

FIG. 4. Dielectron emission rates computed at LO, NLO [11], and NLO plus LO LPM corrections ($\mathrm{LPM_{LO}}$) as well as LPM corrections at NLO ($\mathrm{LPM_{NLO}}$) [12] as a function of the dimensionless quantity M/T for the values $P = 0.53$ GeV and $T = 0.18$ GeV, and the u, d, and s quarks have been considered. These corrections dominate at small total momentum P.

NLO curve. In fact, at NLO, the dilepton emission rate diverges in the limit $M/T \to 0$. This divergence is cured by the LO LPM effect. The fact that the LPM effect at LO is positive for $M > T$ is not so surprising. For $M > T$ the destructive interference effects are not relevant anymore and the LPM effect only takes into account higher-order diagrams that are not included in the NLO calculation. These diagrams happen to give positive contributions to the dilepton rate. The LPM effect at NLO gives an additional positive contribution to the dilepton rate for $M \sim T$, but one can see in Fig. 4 and looking at the asymptotics given in Ref. [12] that it still damps the dilepton rate for $M \ll T$.

C. Geometry of HIC and hydrodynamics of the plasma

Throughout this work we keep the longitudinal dynamics (along the collision axis), separated from the transverse dynamics, described by the $(2+1)$-dimensional hydrodynamic model in Sec. III A [16,17].

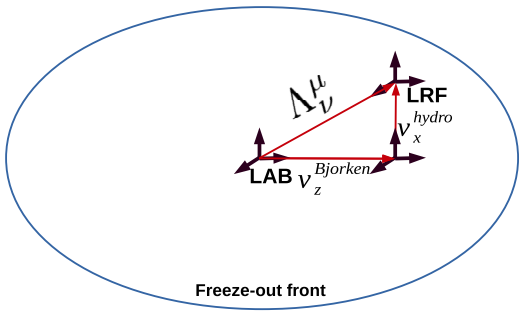

FIG. 5. Scheme of the combination of longitudinal and transverse velocity and the final boost Λ^μ_ν.

We use the Bjorken model [18,19] to describe the longitudinal expansion, and thus we assume the existence of a "central plateau" structure in the production rate of particles as a function of space-time rapidity:

$$\zeta = \frac{1}{2}\ln\frac{t+z}{t-z}. \tag{5}$$

Rapidity ζ and proper time $\tau = \sqrt{t^2 - z^2}$ are therefore a convenient reparametrization of z and t to describe the longitudinal flow:

$$x^\mu = (\tau\cosh\zeta, \mathbf{x}_\perp, \tau\sinh\zeta), \tag{6}$$

so that one can rewrite the differential measure of space-time as $d^4X = \tau d\tau d\zeta d^2x_\perp$.

The longitudinal Bjorken flow [18] velocity is defined simply as the distance covered over proper time:

$$u_\mu(t,z) = \gamma_B(1,0,0,v_z) = \gamma_B\left(1,0,0,\frac{z}{t}\right), \tag{7}$$

where $\gamma_B = \frac{1}{\sqrt{1-(z/t)^2}}$. Furthermore, we obtain the temperature in the $\zeta = 0$ slice, using a $(2+1)$-dimensional hydrodynamic simulation (see Sec. III A).

D. Dilepton spectra in HICs

One can rewrite formula (4) using a new parametrization of the four-momentum of the virtual photon [10], which is better suited for the geometry of HICs:

$$p^\mu = (m_\perp\cosh y, p_\perp\cos\phi_p, p_\perp\sin\phi_p, m_\perp\sinh y). \tag{8}$$

In the formula above, ϕ_p denotes the azimuthal angle, the transverse mass is $m_\perp \equiv \sqrt{M^2 + p_\perp^2}$, and y is the momentum space rapidity:

$$y = \frac{1}{2}\ln\frac{p^0 + p^z}{p^0 - p^z}. \tag{9}$$

Using Eq. (8), we write the differential four-momentum as $d^4P = MdMdyp_\perp dp_\perp d\phi_p$.

We are now ready to compute the invariant mass and rapidity differential spectra:

$$\frac{dN^{l^+l^-}}{MdMdy} = \int_{p_\perp^{\min}}^{p_\perp^{\max}} p_\perp dp_\perp \int_0^{2\pi} d\phi_p \int d^4X \frac{dR^{\ell\bar{\ell}}}{d^4P}. \tag{10}$$

Because we are interested only in the thermal contribution to the dilepton emission spectrum, the integration over d^4X is performed only on the quark-gluon plasma volume, i.e., in the regions with temperature bigger than the critical temperature, $T(\mathbf{x}_\perp,\tau) > T_c = 0.17$ GeV.

It is important to note that, in formula (10), the values of $p_\perp$ are defined in the laboratory reference frame (LAB), but the emission rate dR/d^4P [in formula (4)] has been computed in the local rest frame (LRF) of the plasma [10]. While integrating over the plasma volume, we have to boost the observed LAB frame momenta to the LRF of the plasma, which we can plug into the dilepton rate formula (4) computed previously.

E. Change of reference frame

Let us consider the integral over space-time in Eq. (10) and write it more explicitly using Eq. (6): $\int d^4X \frac{dR^{l^+l^-}}{d^4P} = \int \tau d\tau d\mathbf{x}_\perp d\zeta \frac{dR^{l^+l^-}}{d^4P}$. Notice that the emission rate (4) depends on $\mathbf{x}_\perp$ and τ only through the temperature $T(\mathbf{x}_\perp,\tau)$, which is given by the hydrodynamical simulation, while the dependence on ζ is given by the Bjorken model as anticipated.

At the end of the previous subsection, we noticed that, whenever we fix a LAB frame value of p_μ and a volume element in space in the integral (10), it is necessary to boost the momentum to the LRF of the volume element from which we want to compute the emission rate, see Fig. 5.

To do this, we need the boost $\Lambda^\mu_\nu(u^\mu)$ that parametrizes the change of coordinates from the LAB frame to the LRF [10]. It is defined by the relative velocity $u^\mu_{\rm tot}(x^\mu)$ that combines the Bjorken longitudinal velocity with the transverse hydrodynamical expansion. Once we find $u^\mu_{\rm tot}(x^\mu)$, we are able to compute (10) considering $\frac{dR^{l^+l^-}}{d^4P}[\Lambda^\mu_\nu(u_{\rm tot})p^\nu_{\rm LAB}]$. In what follows, we show the derivation of $u^\mu_{\rm tot}(x^\mu)$.

From the hydrodynamical simulations we obtain the four-velocity of the transverse flow (for $\zeta = 0$),

$$u^\mu_{\rm hydro} = \gamma_{\rm hydro}\{1, v^x_{\rm hydro}, v^y_{\rm hydro}, 0\},$$

where $\gamma_{\rm hydro} = 1/\sqrt{1-(v^i_{\rm hydro})^2} = \sqrt{1+(u^i_{\rm hydro})^2}$ and $v^x_{\rm hydro}$ and $v^y_{\rm hydro}$ are measured with respect to the collision axis. However the whole system is moving along the longitudinal axis with the Bjorken velocity v_B, given by Eq. (7). Thus we need to use the relativistic composition law to find the total velocity with respect to the LAB frame.

The total velocity of a generic element of volume inside the QGP is the relativistic sum of v^z and $\mathbf{v}_{\rm hydro}$.[1]

Applying the relativistic addition rule for perpendicular velocities $\mathbf{v}_{\rm tot} = \mathbf{v}_B + \sqrt{1-v_B^2}\mathbf{v}_{\rm hydro}$, one obtains $u_{\rm tot}(x) = \gamma_{\rm tot}(1, \gamma_B^{-1}v^x_{\rm hydro}, \gamma_B^{-1}v^y_{\rm hydro}, \frac{z}{t})$, where $\gamma_{\rm tot} = \gamma_B\gamma_{\rm hydro}$.

III. NUMERICAL SIMULATIONS

A. SONIC

The collisions between two heavy ions are not well understood at early times, before the system thermalizes. As soon as the QGP is formed (at proper time $\tau_{\rm in} \sim 0.5$ fm), its space-time evolution is described by hydrodynamic models [20].

We simulate the hydrodynamic evolution of the QGP using the software SONIC (Super hybrid mOdel simulatioN for relativistic heavy-Ion Collisions), developed by Romatschke, Luzum, and others (the code is available at the URL listed in Ref. [21]) [16,17,22,23]. In this section we summarize the model which SONIC is based on.

It consists of a $(2+1)$-dimensional model that takes into account only the slice at rapidity $\zeta = 0$, in which the center of mass lies. It combines the pre-equilibrium flow, modeled as in Ref. [24], the hydrodynamic phase with the equation of state from Ref. [25] and the final hadronization [26,27] (which does not concern this work).

SONIC simulates the highly boosted and Lorentz contracted nuclei starting from their thickness function, $T_{tt} = \delta(t+z)T_A(\mathbf{x}_\perp)$, where the function T_A has the following form [17,28]:

$$T_A = \epsilon_0 \int_{-\infty}^{\infty} dz \left[1 + e^{-(\sqrt{\mathbf{x}_\perp^2+z^2}-R)/a}\right]^{-1}, \tag{11}$$

R and a are the charge radius and the skin depth parameters (the values of these parameters can be found in Table 1 in Ref. [17]) and ϵ_0 is a normalization constant that controls the final charged multiplicity and it is set to reproduce the available experimental data.

For a collision with impact parameter $\mathbf{b}$, the pre-equilibrium radial flow velocity is estimated numerically in Ref. [16]:

$$v_i^\perp(\tau,\mathbf{x}_\perp) = -\frac{\tau}{3.0}\partial_i \ln[T_A(\mathbf{x}_\perp)T_A(\mathbf{x}_\perp - \mathbf{b})], \tag{12}$$

where $\tau = \sqrt{t^2-z^2}$. The initial energy profile is set to be

$$\epsilon(\tau,\mathbf{x}_\perp) = T_A(\mathbf{x}_\perp)T_A(\mathbf{x}_\perp - \mathbf{b}). \tag{13}$$

SONIC includes the relativistic viscous hydrodynamics solver (here we use Version 1.7) that implements the evolution of the system using the energy density from Eq. (13) and the flow profile from Eq. (12).

The main parameters that need to be set in the hydrodynamical simulation are the freeze-out temperature $T_c = 0.17$ GeV; the initial central temperature, $T = 0.37$ GeV for the RHIC and $T = 0.47$ GeV for the LHC; and the shear viscosity $\eta/s = 1/4\pi$.

B. Integration of the dilepton rate

In this subsection, we spell out the details of the numerical computation for the dilepton spectra (10).

First we must introduce the setting to the SONIC simulations. The starting proper time is $\tau_{\rm start} = 0.5$ fm and the temporal lattice spacing is 0.001 fm. The space grid (which spans the x-y plane) is made out of 139 lattice sites (per each dimension), separated by $dx = dy = 1$ GeV^{-1}; it covers the squared area $[-13.6, 13.6]^2$ fm^2. Every 500 time steps (0.5 fm), it takes a "snapshot," i.e., it writes into data files the measurable quantities, from which we obtain the temperature and the transverse velocity.

From the inner to outer integration in Eq. (10), we first computed the integration over $\tau d\tau d\zeta$ with the method of

[1]The sum of relativistic velocities is not commutative. According to the Bjorken model, we make the hypothesis that, in the central rapidity plateau, the transverse evolution of the plasma is the same at any rapidity. Thus a generic slice of plasma at a generic rapidity ζ_0 evolves radially exactly like the $\zeta_0 = 0$ slice described by the hydro model. We want to obtain the total velocity of a generic element of volume of the plasma with respect to the LAB frame where p^μ is measured. The LAB frame, in our case, corresponds to the center-of-mass frame, thus every time we fix p^μ in the LAB frame we first have to make a boost along the longitudinal axis to the center of the "ζ_0-plasma slice" and then add the transverse velocity relative to that point, obtained with the hydrodynamics simulations.

parallelepipeds. We integrated ζ in the half range [0,0.9] divided in 20 steps and then doubled the result (the integral is symmetric for positive and negative values of ζ). The other integrals (over the transverse coordinates x and y) were computed separately with the method of trapezes on the same lattice as the SONIC simulation.

The integral $\int d\phi_P$ was computed in $[0,\pi/2]$ with four steps and then we multiplied the result by 4 (the system is symmetric under rotation with period $\pi/2$). The limits of integration for $p_\perp$ for the RHIC simulations were chosen as in the STAR experiment: $p_\perp \in [0.2,15]$ GeV (we note that contributions from $p_\perp > 15$ GeV are negligible). We chose the same $p_\perp$ interval also for the LHC simulations, to facilitate the comparison, and the integral was computed in 33 steps.

The values of $\frac{dR^{l^+l^-}}{d^4P}$ were tabulated in advance as a function of T, M, and $p_\perp$ and the values of M that we plotted always corresponded to nodes of the three-dimensional mesh on which $\frac{dR^{l^+l^-}}{d^4P}$ was tabulated.

The same procedure was not possible for $p_\perp$ because the boost shifts its value. Thus for given $p_\perp$ and T we found the corresponding $\frac{dR^{l^+l^-}}{d^4P}$ by bilinear interpolation.

IV. RESULTS

In this section, we present the results for the invariant mass dependence of the thermal dielectron spectrum (10) of the quark gluon plasma created in Au-Au collisions at $\sqrt{s} = 200$ GeV at the RHIC and for Pb-Pb collisions at $\sqrt{s} = 2.76$ TeV at the LHC. Moreover we compare our results with the experimental data from the STAR experiment.

A. Thermal dilepton emission at the RHIC

Simulating with SONIC the quark gluon plasma created at the RHIC for different impact parameters b, we have access to the temperature and fluid velocity dependence of the plasma. Using this data, we can calculate the thermal dilepton spectrum (10) as a function of the invariant mass M, for different values of the impact parameter b and for LO, NLO, and NLO + LPM approximations. These results are shown in Fig. 6.

The STAR experiment measures the electron-positron pairs from Au-Au ions collisions at $\sqrt{s} = 200$ GeV, as a function of the invariant mass M of the virtual photon [5]. The STAR experiment can capture emitted leptons at all azimuthal angles and with momentum-space rapidity values $|y| < 1$. To make a good comparison with the experiment, we also integrate the dilepton spectrum over momentum-space rapidity values $|y| < 1$. Moreover, the data are classified by centrality ranges; thus it is necessary to average our results over the impact parameter b to reproduce the centrality dependence. To achieve this, we integrate over different impact parameters b as[2]

$$\frac{dN}{dM}(\%\ \text{centrality}) = \frac{\int_{b_{\min}}^{b_{\max}} dbb\frac{dN}{dM}(b)}{\int_{b_{\min}}^{b_{\max}} dbb}, \tag{14}$$

where $b_{\min}$ and $b_{\max}$ can be found as a function of centrality in Refs. [29,30].[3] Figure 7 shows the dilepton spectrum for the RHIC averaged on all the centralities 0–80%, which, for Au-Au collisions, corresponds to $b = 0$–13 fm, for different orders in perturbation theory.

Of course, the experimental data from Ref. [5] include, in addition to the thermal dileptons, high energetic electron-positron pairs from pre-equilibrium processes and mainly the

[2]The integral over y and the one in the numerator of Eq. (14) have been computed with Simpson's rule for parabolic integration. Considering the dependence of the emission rate on the impact parameter (see Refs. [29,30]), this should give the exact solution of the integral in the range $b \in [0,13]$ fm.

[3]Analog tables for the LHC are in Ref. [31].

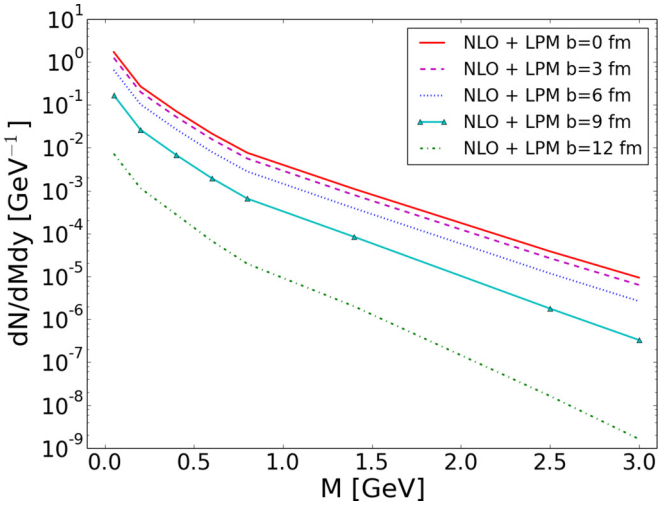

FIG. 6. Invariant mass spectra for the dilepton emission at the RHIC computed at NLO with LPM (at NLO) corrections for different values of the impact parameter b, for central rapidity $y = 0$, and for transverse momentum $p_\perp \in [0.2,15]$ GeV.

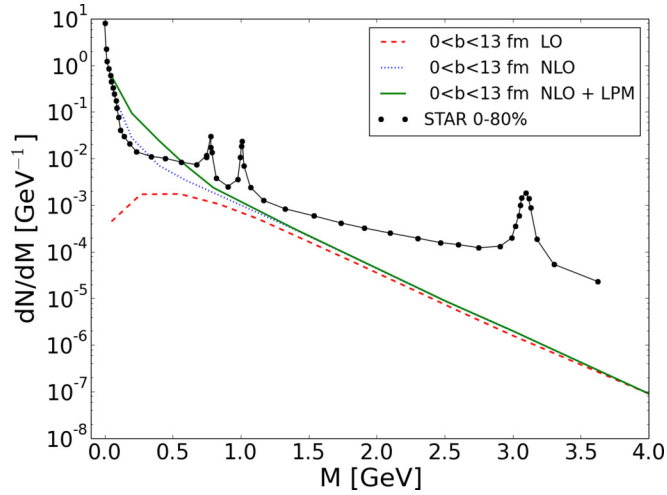

FIG. 7. Invariant mass spectrum for the emitted emitted dileptons computed at LO, NLO, and NLO + LPM corrections for the full detected centrality range (0–80%) and comparison with the relative data from the STAR experiment. Error bars for the STAR data can be found in Ref. [5].

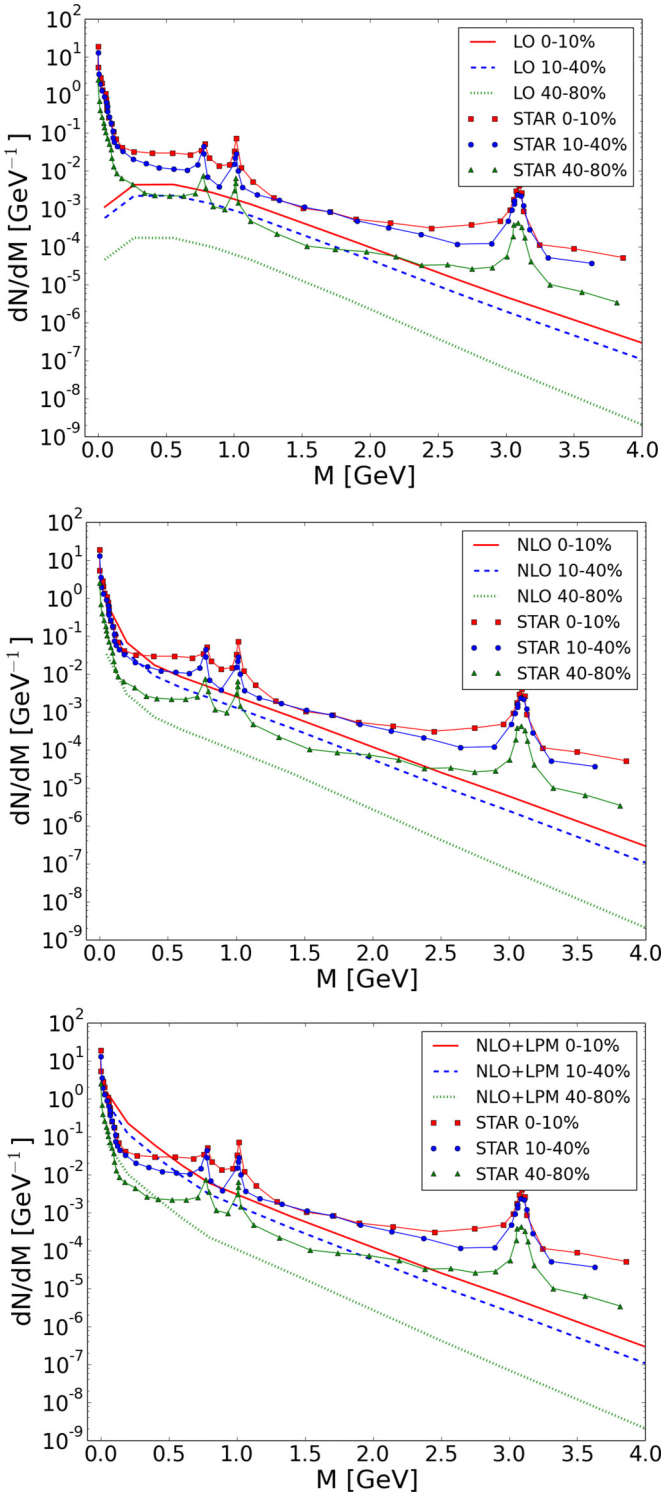

FIG. 8. From top to bottom: Invariant mass spectra for the dilepton emission at the RHIC computed at LO, NLO, and NLO with LPM (at NLO) corrections, respectively, for different ranges of centrality. In each plot our calculations are compared with the relative data from STAR. The predicted spectra includes the rapidity range $|y| < 1$ and the transverse momentum range $p_\perp \in [0.2, 15]$ GeV.

ones generated in the following decays: $\omega \to e^+e^-\pi^0$; $\pi^0 \to e^+e^-\gamma$; $\eta \to e^+e^-\gamma$,η^0; $\omega \to e^+e^-$; $\rho \to e^+e^-$; $\phi \to e^+e^-$; and $J/\psi \to e^+e^-X$. For large invariant mass, the thermal contribution quickly becomes small compared to the other contributions discussed in the Introduction [6–9]. In the high mass range $2 < M < 3$ GeV, the contribution from particle decays is much more important than the thermal one. For $M > 3$ GeV the main contribution to the spectrum is given by dielectron couples produced in pre-equilibrium Drell-Yan processes, and our forecasts are, of course, much smaller than the experimental data.

The region in which the thermal contribution is dominant is indeed very small, i.e., roughly $0.2 < M < 1.5$ GeV, up to the ρ, ω, and ϕ peaks. In this region the agreement can be tested.

Figure 8 shows the comparison between our calculations and the experimental data for different ranges of centrality, computed as in Eq. (14). Surprisingly, the LPM corrections overestimate the number of emitted thermal dileptons at small invariant mass and the NLO approximation is the closest to the experimental data. In the very low mass range $M < 0.5$ GeV, perturbation theory breaks down and a different approach is required, for example, lattice simulations.

For $M > 0.7$ GeV, our results are a bit smaller than the experimental data as expected, since we do not consider all the contributions that are included in the experimental data. Moreover, we can notice that, for large impact parameter b, the agreement between the calculations and the experimental data becomes poor. This is expected, because for large b the volume of the produced plasma is smaller and so the thermal contribution to the invariant mass dilepton spectrum is less important.

B. Thermal dilepton emission at LHC

A similar analysis can be carried out for the LHC. Figures 9–11 are the analog of Figs. 6–8 but for Pb-Pb collisions at

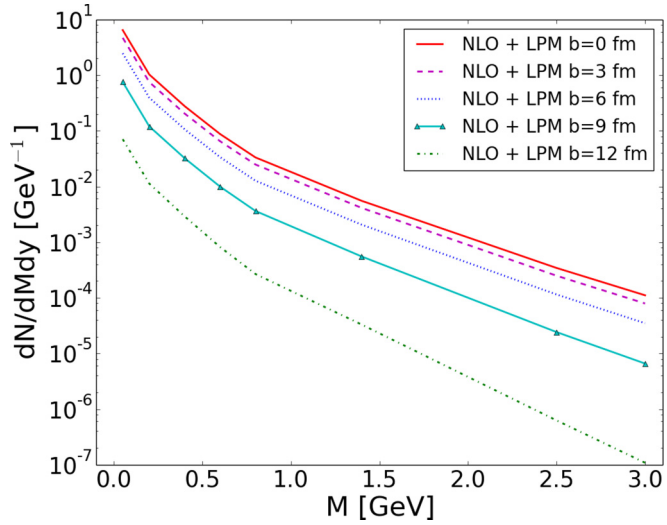

FIG. 9. Invariant mass spectra for the dilepton emission at the LHC computed at NLO with LPM (at NLO) corrections for different values of the impact parameter b. The curves are computed at midrapidity $y = 0$, for the transverse momentum range: $p_\perp \in [0.2, 15]$ GeV.

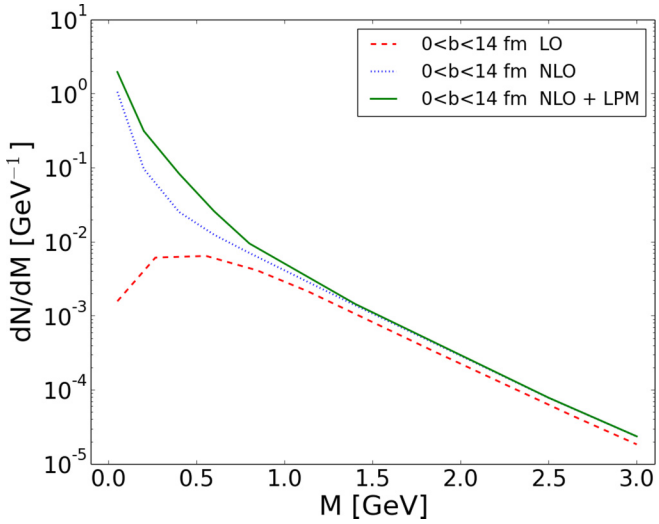

FIG. 10. Invariant mass spectra for the dilepton emission at the LHC computed at LO, NLO, and NLO with LPM corrections for collisions with centrality in the range 0–80%. The curves are computed for $|y| < 1$, for the transverse momentum range: $p_\perp \in [0.2, 15]$ GeV.

$\sqrt{s} = 2.71$ TeV at the LHC. In the absence of experimental results, we kept the same cuts ($y < 1$, $p_\perp \in [0.2, 15]$) as for the comparison to the STAR experiment. This allows for a physical comparison between the rates at the LHC and the RHIC.

We notice that the slope of the spectra between $M = 1$ and $M = 3$ GeV is less steep for the LHC spectrum than for the RHIC spectrum. In fact, around $M = 1$ GeV, the LHC spectrum is 4 times bigger than the one at the RHIC, but for $M = 3$ GeV it is almost 12 times bigger.

Again, at large invariant mass, different processes will contribute to the dilepton emission rate [6–9] and the thermal dilepton emission will be a small effect. However, at small invariant mass (but larger than the pion mass), we expect that the thermal emission will dominate at the LHC, opening a window where we can compare the different estimates for the dilepton rate to experiment.

As a last remark, one can further integrate over the invariant mass M to obtain the total number of dilepton pairs produced thermally in one collision. If we average over centrality 0–80% and include NLO + LPM corrections, we obtain 0.57 pairs for the LHC and 0.22 for the RHIC.

V. CONCLUSION

The main result of this work is the comparison between the thermal dilepton rate calculated at LO, NLO, and NLO + LPM. The higher-order corrections become important for small values of the invariant mass of the virtual photon M. Comparing our results with experimental data from the STAR experiment at the RHIC, we see that for small invariant mass the NLO + LPM rate seems to overshoot the data. This shows that the LPM effect, even if it damps the rate at very small M, actually enhances the rate for $M \sim 0.5$ GeV too much to be compatible with the STAR experiment. The NLO seems to fit

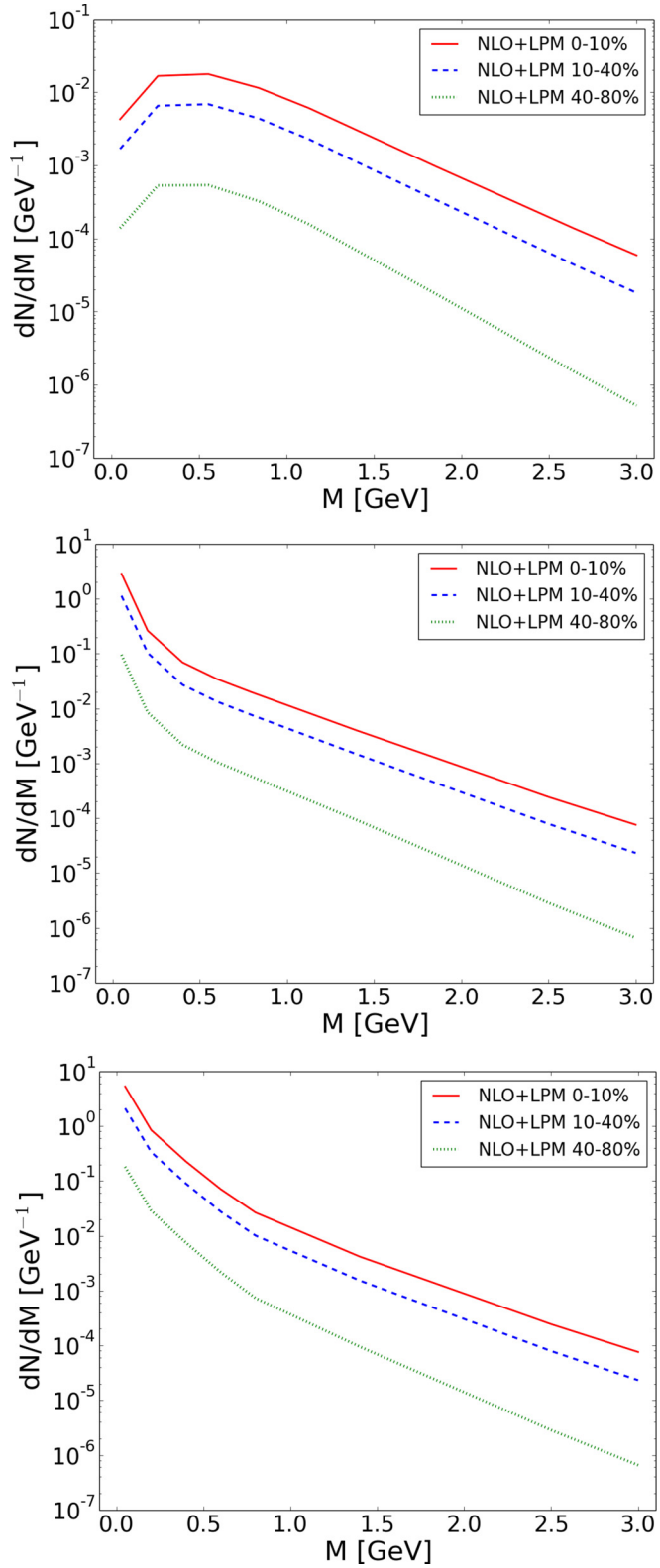

FIG. 11. From top to bottom: Invariant mass spectra for the dilepton emission at the LHC computed at LO, NLO, and NLO + LPM corrections for different ranges of centrality. The curves are computed for $|y| < 1$, for the transverse momentum range: $p_\perp \in [0.2, 15]$ GeV.

experiment best but overshoots the data for $M < 0.5$ GeV. We see there is a motivation for additional experimental and theoretical studies of the dilepton emission rate. In fact, for small values of M it seems that a nonperturbative determination is a must.

We also performed calculations of the thermal dilepton emission at the LHC, where the plasma phase might become more important in comparison to other sources. Results from the LHC would be very useful to settle the tension between the STAR data and higher-order calculations of the dilepton rate.

ACKNOWLEDGMENTS

We would like to thank Jacopo Ghiglieri for useful discussions. Y.B. is supported by the Swiss National Science Foundation (Grant No. PZ00P2-142524).

[1] J. Adams *et al.* (STAR Collaboration), Nucl. Phys. A **757**, 102 (2005).
[2] K. Adcox *et al.* (PHENIX Collaboration), Nucl. Phys. A **757**, 184 (2005).
[3] L. D. McLerran and T. Toimela, Phys. Rev. D **31**, 545 (1985).
[4] Y. Akiba (PHENIX Collaboration), Nucl. Phys. A **830**, 567c (2009).
[5] F. Geurts (STAR Collaboration), J. Phys.: Conf. Ser. **458**, 012016 (2013).
[6] E. L. Bratkovskaya, Nucl. Phys. A **931**, 194 (2014).
[7] G.-M. Yu and Y.-D. Li, Phys. Rev. C **91**, 044908 (2015).
[8] G. Vujanovic, C. Young, B. Schenke, S. Jeon, R. Rapp, and C. Gale, Nucl. Phys. A **904-905**, 557c (2013).
[9] G. Vujanovic, C. Young, B. Schenke, R. Rapp, S. Jeon, and C. Gale, Phys. Rev. C **89**, 034904 (2014).
[10] R. Ryblewski and M. Strickland, Phys. Rev. D **92**, 025026 (2015).
[11] I. Ghisoiu and M. Laine, J. High Energy Phys. 10 (2014) 083.
[12] J. Ghiglieri and G. D. Moore, J. High Energy Phys. 12 (2014) 083 .
[13] H. A. Weldon, Phys. Rev. D **42**, 2384 (1990).
[14] J. I. Kapusta and C. Gale, *Finite-Temperature Field Theory: Principles and Applications*, Cambridge Monographs on Mathematical Physics (Cambridge University Press, Cambridge, UK, 2011).
[15] Laine's database is available at http://www.laine.itp.unibe.ch/dilepton-lpm/.
[16] W. van der Schee, P. Romatschke, and S. Pratt, Phys. Rev. Lett. **111**, 222302 (2013).
[17] M. Habich, J. L. Nagle, and P. Romatschke, Eur. Phys. J. C **75**, 15 (2015).
[18] J. D. Bjorken, Phys. Rev. D **27**, 140 (1983).
[19] G. Roland (for the PHOBOS Collaboration), Nucl. Phys. A **774**, 113 (2006).
[20] C. Nonaka and M. Asakawa, Prog. Theor. Exp. Phys. **2012**, 01A208 (2012).
[21] Source codes are available at https://sites.google.com/site/revihy/.
[22] P. Romatschke and U. Romatschke, Phys. Rev. Lett. **99**, 172301 (2007).
[23] M. Luzum and P. Romatschke, Phys. Rev. C **78**, 034915 (2008).
[24] R. Baier, P. Romatschke, D. T. Son, A. O. Starinets, and M. A. Stephanov, J. High Energy Phys. 04 (2008) 100.
[25] M. Laine and Y. Schroder, Phys. Rev. D **73**, 085009 (2006).
[26] J. Sollfrank, P. Koch, and U. W. Heinz, Z. Phys. C **52**, 593 (1991).
[27] J. Sollfrank, P. Koch, and U. W. Heinz, Phys. Lett. B **252**, 256 (1990).
[28] P. Romatschke, Int. J. Mod. Phys. E **19**, 1 (2010).
[29] K. Reygers (unpublished), available at http://www.phenix.bnl.gov/∼enterria/tmp/glauber/glauber_auau_200gev.pdf.
[30] D. Kharzeev and M. Nardi, Phys. Lett. B **507**, 121 (2001).
[31] B. Abelev *et al.* (ALICE Collaboration), Phys. Rev. C **88**, 044909 (2013).